Effect of Nanostructuring and Ex situ Amorphous Carbon Coverage on the Lithium Storage and Insertion Kinetics in Anatase Titania

Shyamal K. Das, Manu Patel, and Aninda J. Bhattacharyya*

Solid State and Structural Chemistry Unit, Indian Institute of Science, Bangalore 560012, India

ABSTRACT Implications of nanostructuring and conductive carbon interface on lithium insertion/removal capacity and insertion kinetics in nanoparticles of anatase polymorph of titania is discussed here. Sol−gel synthesized nanoparticles of titania (particle size ∼6 nm) were hydrothermally coated ex situ with a thin layer of amorphous carbon (layer thickness: 2−5 nm) and calcined at a temperature much higher than the sol−gel synthesis temperature. The carbon-titania composite particles (resulting size ∼10 nm) displayed immensely superior cyclability and rate capability (higher current rates ∼4 A g^{-1}) compared to unmodified calcined anatase titania. The conductive carbon interface around titania nanocrystal enhances the electronic conductivity and inhibits crystallite growth during electrochemical insertion/removal thus preventing detrimental kinetic effects observed in case of unmodified anatase titania. The carbon coating of the nanoparticles also stabilized the titania crystallographic structure via reduction in the accessibility of lithium ions to the trapping sites. This resulted in a decrease in the irreversible capacity observed in the case of nanoparticles without any carbon coating.

KEYWORDS: anatase titanium dioxide • nanoparticles • carbon coating • insertion • percolation • lithium-ion battery

1. INTRODUCTION

Titanium dioxide (TiO_2) has been successfully demonstrated as a prospective material for a variety of applications such as catalysis (1), photovoltaics (2), and sensing (3). Recently, TiO_2 (and TiO_2 based materials such as $Li_4Ti_5O_{12}$) have also been demonstrated as promising anodes in rechargeable lithium ion batteries (4−9). In comparison to conventional carbonaceous anode materials, TiO_2 has a lithium insertion voltage at approximately 1.5 V, which is far above the lithium plating voltage (∼100 mV) and thus leading to safer lithium-ion batteries. Additionally, TiO_2 is chemically stable, environmentally benign and cheap. Among the various polymorphs of TiO_2, anatase and TiO_2 (B) in recent times have been extensively investigated as anode in lithium batteries (4). Because of low packing density, anatase (density, $\rho = 3.89$ g cm^{-3}) and TiO_2 (B) ($\rho = 3.73$ g cm^{-3}) phases show higher lithium storage compared to densely packed brookite ($\rho = 4.13$ g cm^{-3}) and rutile ($\rho = 4.25$ g cm^{-3}) phases (4). However, against this conventional thought, Dambournet et al. recently demonstrated that rutile and brookite (porous) titania can also store lithium equivalent to the anatase polymorph (10). Additionally, nanostructuring of anatase and TiO_2 (B) phases have led to further enhancement in electrochemical performance. Nanotubes, nanowires, and various other nanostructures of anatase and TiO_2 (B) have shown near theoretical specific capacities (= 335 mA h g^{-1}) and improved rate capabilities (5). The improved performance resulting out of nanostructuring is ascribed to reduced diffusion path lengths for the conducting species and larger electrode/electrolyte contact area which facilitates easier lithium insertion/removal (11−13). However, poor electronic conductivity of TiO_2 (∼1×10^{-12} Ω^{-1} cm^{-1}) (14, 15) compared to carbon limits it is usage in lithium ion battery. For better rate capability, the intercalating host must be a good ionic as well as an electronic conductor. Several opportunities exist for the optimization of these intrinsic parameters (16−20). An often employed approach for improving electronic conductivity has been to optimize host particle size and shape or coat titania particle surface either during or post synthesis with conductive additives such as carbon. The electron transport is enhanced primarily due to the formation of a percolating arrangement of carbon and intercalating host (active) particles. A serious drawback associated with nanometer sized particles is that repeated Li insertion/removal leads to particle agglomeration due to high surface energy. As a result benefits of the nanoscale are lost and this is manifested via poor battery cycling performance. The aggregation problem has been dealt in extensive detail worldwide by several research groups (21−23). The approach here too involves coating of nanoparticles by a second phase material and organization of the particles in a porous network. Furthermore, as emphasized by P. Novak and his co-workers, homogeneity in the network comprising the conductive additives and intercalating host nanoparticles is a prerequisite for high-power lithium batteries (24). Therefore, in situ grown homogeneous conductive coating such as hydrothermally grown carbon

* Corresponding author. E-mail: aninda_jb@sscu.iisc.ernet.in. Tel: +918022932616. Fax: +918023601310.
Received for review April 18, 2010 and accepted June 17, 2010

DOI: 10.1021/am1003409

can simultaneously solve the problems related to percolation and aggregation associated with nanostructured lithium insertion materials. Importantly optimization of the additive carbon is found to be very crucial for high rate performance as demonstrated recently in refs 25 and 26.

We report here a systematic and detailed study concerning the influence of nanostructuring and carbon coating on the lithium storage and insertion kinetics in anatase TiO_2. The problem of nanoparticle agglomeration and beneficial effect of carbon along with trivial size effects are discussed in the context of high current rate galvanostatic cycling performance. A simple one-step procedure was employed to synthesize nanoparticulate anatase TiO_2 and carbon coating was done post TiO_2 synthesis using an optimized hydrothermal method. All synthesized materials were characterized using X-ray diffraction, transmission electron microscopy, thermogravimetry analysis, and N_2 adsorption/desorption isotherms. Electrochemical studies in the form of cyclic voltammetry and galvanostatic cycling at various current rates were done to investigate the lithium insertion kinetics.

2. EXPERIMENTAL SECTION: MATERIALS AND METHODS

Synthesis and Characterization of TiO_2. Anatase TiO_2 nanoparticles were synthesized by a simple one step method similar to that reported in ref 27. Titanium tetraisopropoxide (TTIP, Spectrochem Pvt. Ltd. Mumbai) was used as the titania precursor. In a typical synthesis, 2.73 mL of TTIP is dissolved in 100 mL of ethanol. This transparent solution was slowly added to 100 mL of distilled water maintained at 80 °C and stirred continuously. The reaction was continued for 1 h at 80 °C. The resultant white product was recovered by centrifugation and washed with deionized water and ethanol several times and dried at 100 °C for 24 h. The dried product was further calcined at 400 °C for 4 h under air at a heating rate of 2 °C min^{-1}. Carbon coated TiO_2 nanoparticles were synthesized by hydrothermal treatment of the synthesized TiO_2 nanoparticles (100 mg) in 0.2 M aqueous sucrose solution at 150 °C for 6 h. The black product after recovery via centrifugation was washed several times with ethanol and water. It was dried at 100 °C and annealed at 400 °C for 4 h under N_2 atmosphere at a heating rate of 2 °C min^{-1}. All synthesized materials were stored in an evacuated desiccator until further usage. The materials were designated as T100, T400, and TC400, corresponding to the as synthesized product dried at 100 °C, calcined product at 400 °C, and the carbon-coated TiO_2 nanoparticle, respectively.

The crystallographic phase identification of the products was performed using powder X-ray diffraction (XRD; Philips X'Pert Pro diffractometer; Cu−K_α radiation, $\lambda = 1.5418$ Å) with step width and scan rate of 0.02 and 1.2° per min, respectively. The particle size and morphology before and after galvanostatic cycling was observed by transmission electron microscopy (TEM, FEI Technai T20; accelerating voltage 200 kV). Specific surface area (BET) and pore-size distribution were obtained from nitrogen adsorption−desorption isotherms (Belsorp). Estimation of carbon content and thermal stability of TiO_2 nanoparticles was done using thermogravimetric analysis (TGA, Mettler Toledo). TGA experiments were done by heating the sample in air from room temperature (30 °C) to 850 °C at a heating rate of 5 °Cmin^{-1}.

Electrode Preparation and Electrochemical Characterization. For the working electrode, slurry of active material was prepared with carbon black (Alfa Aesar) and PVdF (Kynarflex) in a weight ratio of 80:10:10 in *N*-methyl-pyrrolidone (NMP). The slurry was cast on a copper foil (Alfa Aesar, thickness =0.05 mm) and dried in vacuum at 120 °C for 20 h. The weight of active materials varied between 1.5 and 2.5 mg for each cell. Room temperature cyclic voltammetry (CV) and galvanostatic charge/discharge cycling were done in Swagelok cells with pure metal Li (Aldrich) as anode, Whatman glass fiber as separator and 1 M $LiPF_6$ in ethylene carbonate (EC, Aldrich) and dimethyl carbonate (DMC, Aldrich) (1:1 w/w) as electrolyte. All cell assembly was done at 25 °C in a glovebox (MBraun) under argon (H_2O: < 0.1 ppm). The voltage ranges for CV and galvanostatic cycling were respectively 1−2.5 V (scan rate: 0.1 mV s^{-1}) and 1−2.5 V (versus Li^+/Li). For ex situ XRD measurements, requisite number of galvanostatic charge/discharge cycling was performed at a constant current rate of 75 mA g^{-1}. The cells were disassembled inside argon filled glovebox and the (charged/discharged) electrodes were cleaned repeatedly with a solution of EC/DMC (1:1 w/w). They were dried and stored in the glovebox until further use. Electrochemical impedance spectroscopic analysis (EIS) was conducted using Alpha Novocontrol equipment by applying an ac stimulus with 0.01 V of amplitude and no applied bias voltage in the frequency range of 200 kHz to 10 mHz. The impedance response was measured before cycling (at open circuit potential) and after first discharge cycle (current rate = 75 mA g^{-1}). For reproducibility, nearly three cells per sample were run simultaneously. All electrochemical data were within ±5%. All electrochemical measurements were carried out using Arbin Instruments (MSTAT).

3. RESULTS AND DISCUSSION

All synthesized and calcined products showed broad X-ray diffraction peaks which can be indexed to anatase phase with lattice parameters $a = b = 3.7852$ Å, $c = 9.5139$ Å, and space group $I4_1/amd$ (141) (JCPDS No. 21−1272) (see the Supporting Information, Figure 1). In the case of XRD (see the Supporting Information, Figure 1c) of TC400, no peak shift was observed, suggesting the absence of chemical bonding or reaction between the carbon material and TiO_2 nanoparticles. Furthermore, no characteristic peak from carbon was detected in XRD strongly indicating the formation of amorphous carbon. The broad diffraction peaks in all cases are attributed to the small size of the TiO_2 crystallites. From the full width at half-maximum (fwhm) for the (101) peak ($2\theta = 25.50°$), the crystallite size using Scherrer equation is estimated to be approximately 5.6 nm (fwhm = 1.444°) for T100 and 10 nm (fwhm = 0.822°) for T400 and TC400. The formation of bigger crystallites in case of T400 and TC400 is attributed to temperature induced crystallization. It must be mentioned here that the annealing temperature of 400 °C was selected to prevent phase transitions from anatase to rutile (28).

The nitrogen adsorption−desorption isotherms (supporting Figure 2a) of all the materials exhibit type IV isotherm with type H2 hysteresis loop signifying existence of mesopores (29). The BET surface area of T100, T400, and TC400 are 240, 85, and 100 m^2 g^{-1} respectively. Though the crystallite size of T400 and TC400 are the same, the BET surface area of TC400 is higher than T400. This is attributed to the presence of micropores in the hydrothermally grown carbon layer (30). The pore size distribution plot estimated using BJH method (31) shows that the distribution of pore

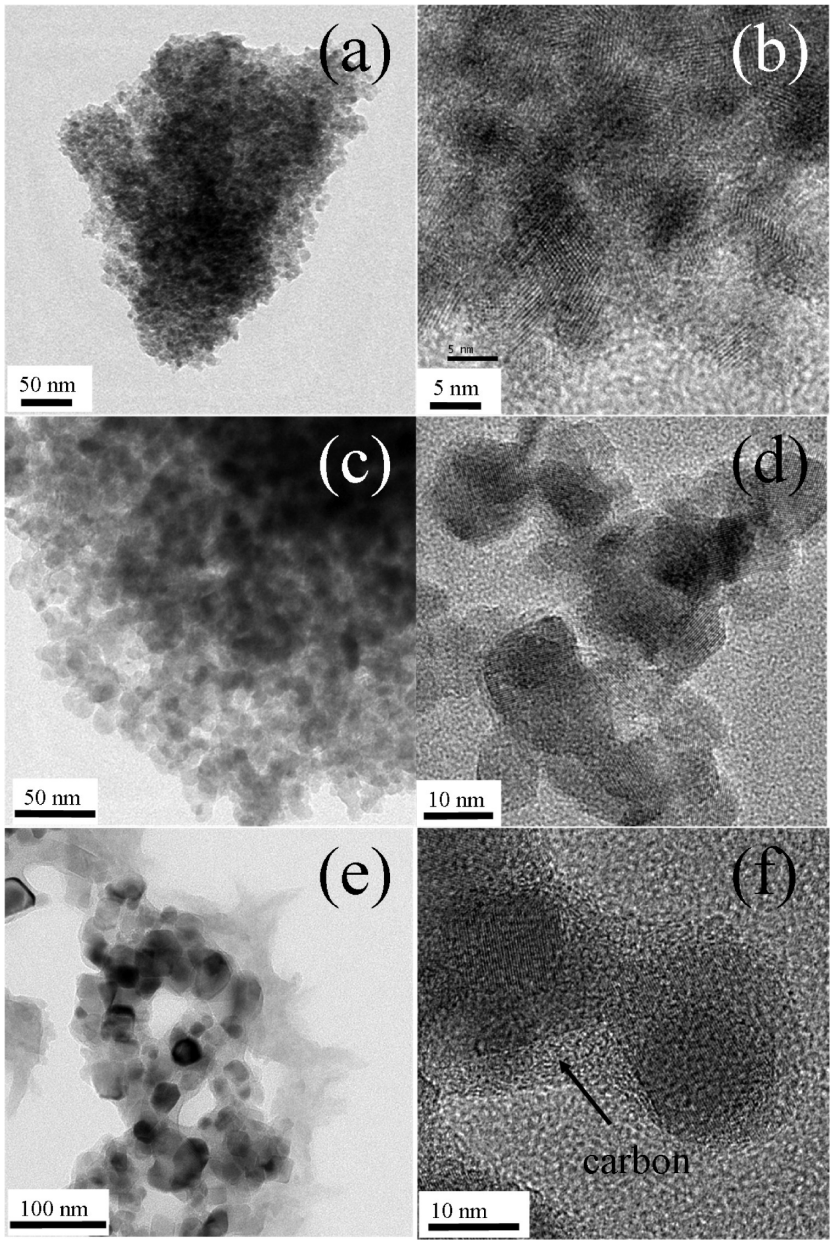

FIGURE 1. Transmission electron micrographs (before cycling) for (a, b) T100, (c, d) T400, and (e, f) TC400. The amorphous carbon shell present in TC400 is indicated by the arrow.

size and shape is not well-defined (see the Supporting Information, Figure 2b). It must be noted here that the synthesis has been carried out without any structure directing agents (such as surfactants) typically used for synthesizing mesoporous materials such as MCM41/48 (32). Therefore, the existence of mesopores in the final products can be reasonably attributed to the spacing between the nanoparticles comprising the aggregates. The formation of TiO_2 porous aggregates is also quite evident from the TEM images shown in Figure 1. Images a and b in Figure 1 and images c and d in Figure 1 correspond to T100 and T400, respectively. From the HRTEM images (Figure 1b, d), it is clear that TiO_2 nanoparticles of size 5−6 nm and 9−11 nm form the TiO_2 aggregates. The presence of homogeneous uniform amorphous carbon coating around TiO_2 particles in TC400 can be observed in the TEM images e and f in Figure 1. The carbon shell thickness is approximately 2−5 nmm as evident from the HRTEM image in Figure 1f. The final particle size for the carbon coated titania was 10 nm. It has been generally observed that coating of small crystallites by a second phase inhibits growth of the crystallites during annealing process (22, 28). However, in the present case, the TiO_2 nanoparticles are in agglomeration with broad pore size distribution (see the Supporting Information, Figure 2b) prior to carbon treatment. Therefore during the hydrothermal carbonization process (from carbohydrates), amorphous carbon initially starts growing in the available mesopores and not over individual TiO_2 nanoparticles. Consequently, the TiO_2 nanoparticles also start growing because of temperature-induced crystallization and get coated with carbon with the simultaneous retention of a mesoporous structure (as evident from pore size distribution, see the Supporting

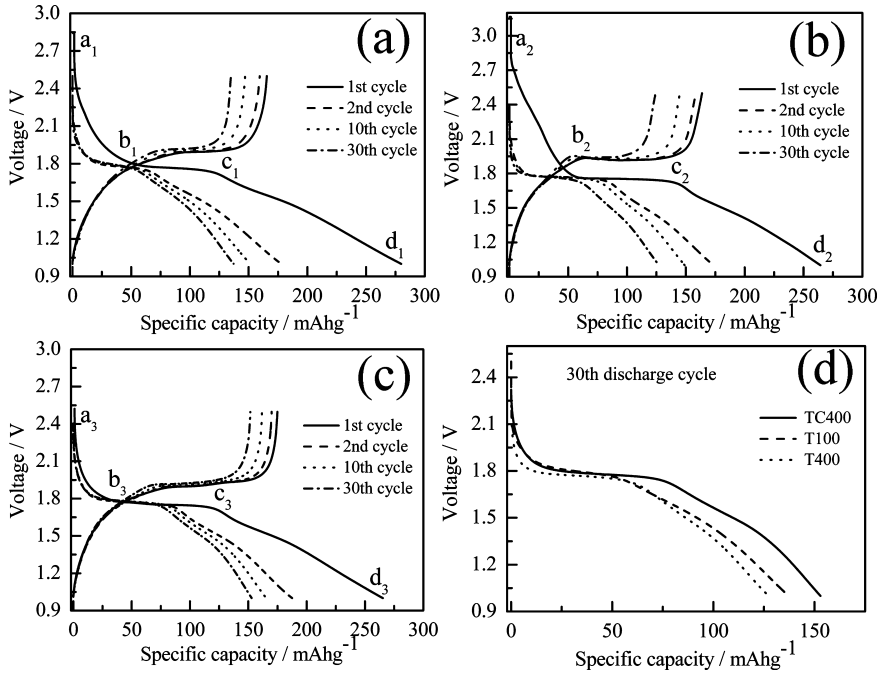

FIGURE 2. Galvanostatic charge−discharge curves of (a) T100, (b) T400, and (c) TC400 at a current density of 75 mA g^{-1} at room temperature (25 °C), (d) comparison of the 30th discharge cycle profile of all materials.

Information, Figure 2b). All the primary particle sizes as observed from the TEM images are in fairly good agreement with sizes estimated from XRD.

The dehydration process of T100, T400, and carbon content in TC400 were investigated using thermogravimetric analysis (TGA) (see the Supporting Information, Figure 3). TGA plot shows two step dehydration processes in case of T100, representing a weight loss of 5% (between 30−150 °C) and 4% (between 150−800 °C). The first step weight loss is attributed completely to the physiadsorbed water on the titania surface and the second step corresponds to the decomposition of residual organic impurities present in T100. However, there is only one-step weight loss in case of T400, which signifies that the weight loss is entirely due to physiadsorbed water. Similar to T100, TC400 exhibited a two-step dehydration processes. The weight loss below 150 °C is attributed to the physiadsorbed water, whereas weight loss in between 150 and 800 °C is due to the decomposition of the amorphous carbon. The weight loss in the range 150−800 °C was estimated to be approximately 12 wt % of the total weight.

Electrochemical Analysis and Lithium Battery Performance Studies. Figure 2 shows the galvanostatic charge (Li removal)/discharge (Li insertion) profiles obtained from T100, T400, and TC400 at a current density of 75 mA g^{-1} at room temperature (25 °C). The Li ion insertion/removal reaction in TiO_2 proceeds according to the following reversible reaction: $TiO_2 + xLi^+ + xe^- \Leftrightarrow Li_xTiO_2$. The maximum value of x ranges from 0.5 to 1 depending on the temperature and experimental conditions (theoretical capacity of $TiO_2 = 335$ mA h g^{-1} corresponding to $x = 1$) (33−35). The kinetics of lithium insertion/removal reaction and consequently the lithium storage capacity is not only dependent on the crystallite size of TiO_2, but it also shows strong dependence on the conductive carbon coating. The permeation of lithium ions to the active material TiO_2 in case of TC400 takes place through the micropores available particularly in amorphous carbon layer (30). T100 exhibited a discharge capacity of 279 mA h g^{-1} in the first discharge cycle, whereas it is 264 and 265 mA h g^{-1} for T400 and TC400, respectively. The capacities for T400 and TC400 are same owing to their identical particle size. This demonstrates that conductive carbon coating over TiO_2 nanoparticles is not beneficial in enhancing the initial lithium storage at low current rates. Structure of the storage material and changes resulting out of nanostructuring influences initial lithium storage. However, one observes significant changes in cycle stability and lithium storage at high current rates due to carbon coating. Similar to as reported for anatase TiO_2 (7), here too one observes the existence of irreversible capacity between first discharge cycle and first charge cycle and reversible capacity between first and second discharge cycle in all cases. However, the magnitude of loss is dependent on the particle size and on carbon coating. The irreversible capacity values are 114, 101, and 90 mA h g^{-1} for T100, T400, and TC400, respectively, which corresponds to Coulombic efficiencies (ratio of extraction to insertion capacity) of 59, 61, and 66%, respectively. Such irreversible capacity loss solely due to formation of solid electrolyte interface (SEI) can be ruled out from the single semicircle ac-impedance spectra (supporting Figure 4) (6). After 30 cycles, the discharge capacities are 137, 127, and 153 mA h g^{-1} with Coulombic efficiencies of 97.6, 97.5, and 99% for T100, T400, and TC400, respectively. It is well-known that nanoparticles possesses high surface energy compared to bulk and can aggregate easily either during synthesis or during the galvanostatic cycling. In the present case, the synthesized TiO_2 nanoparticles form porous aggregates during the

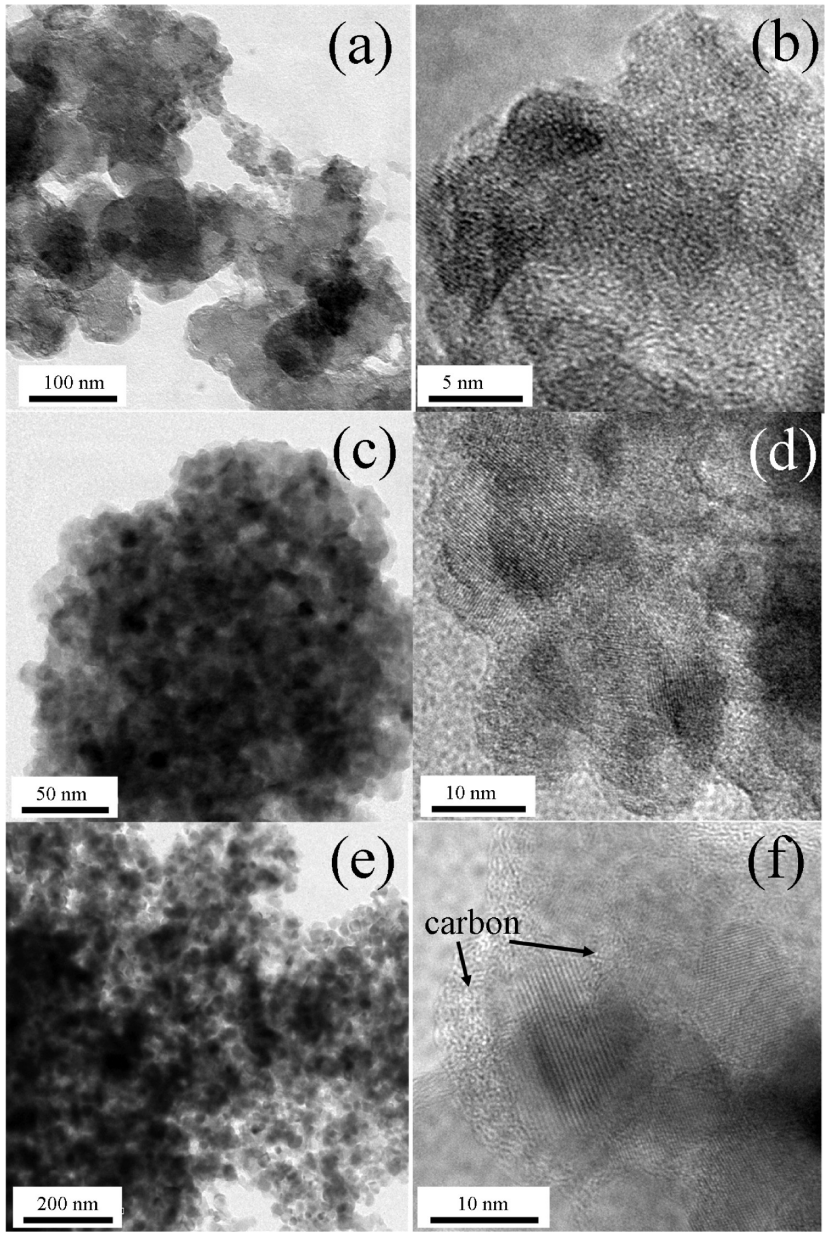

FIGURE 3. Transmission electron micrographs (after cycling) for (a, b) T100, (c, d) T400, and (e, f) TC400. The amorphous carbon shell present in TC400 is indicated by the arrows.

synthesis itself. In addition, repeated charge/discharge cycling results in nanoparticle agglomeration effectively leading to growth of TiO_2 particle size. This adverse effect is observed in the form of gradual capacity fading in case of T100 and T400 as shown in a and b in Figure 2 and in Figure 4. The post cycling TEM images taken after the 80th cycle is shown in Figure 3 and provides evidence of the extent of stability of the different TiO_2 nanoparticles. It can be observed from the TEM images of Figure 3a–d that TiO_2 crystallites undergo further particle agglomeration accompanied with particle growth. Since the primary TiO_2 crystallite size in T400 (particle size ~10 nm) is larger than that of T100 (particle size ~5.6 nm), it is expected that the cycle stability of T400 will be better compared to T100 owing to lower free surface energy and hence lower degree of agglomeration upon cycling. In spite of lower aggregation the degree of capacity fading for T400 is higher than that of T100

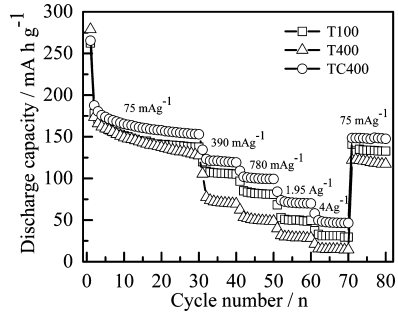

FIGURE 4. Variation in discharge capacity of T100, T400, and TC400 as a function of different current densities (0.075–4 A g^{-1}).

(a and b in Figure 2 and Figure 4). The poor performance in this case can be mainly attributed to larger particle size of T400 (lower surface:volume ratio). It is observed that TC400 (particle size ~10 nm) exhibited superior performance in

terms of cycle stability and storage capacity (Figures 2c and 4). Improved capacity retention in the carbon coated TiO_2 nanoparticles is clearly due to the presence of conductive layer coating which significantly enhances the electronic conductivity via formation of effective percolating network of conductive carbon around the titania nanoparticles. In addition to enhancing the electronic conductivity it also helps in avoiding particle agglomeration as demonstrated by the post cycling TEM images e and f in Figure 3. TC400 retain its initial porous aggregate nature and TiO_2 crystallites are still covered by the amorphous carbon layer after cycling. The utility of carbon coating can also be observed in the rate capability comparison of T400 and TC400 (Figure 4). TC400 showed better rate capability than T400 and T100. So the combination of prevention of particle agglomeration and carbon coating results in superior electrochemical performance of TC400 over T400. The benefits of carbon coating will be manifested even higher for a smaller-sized particle than obtained in the case of TC400. We would like to highlight here that nanoparticle agglomeration have been demonstrated to play a very important role in determining the cycling stability in alloy based electrode materials (e.g., Si, Sn, SnO_2) where huge volume expansion occurs during lithium alloying/dealloying process.

The discharge curves in Figure 2a−c can be divided into three regions marked as *ab*, *bc*, and *cd*. Significant differences are observed in these regions between materials under study. There are two distinct potential plateaus at 1.77 and 1.91 V vs Li^+/Li for discharging and charging processes respectively for all materials similar to that reported in literature (36). In the first discharge process, the potential decreases monotonously (region *ab*) and reaches the plateau at 1.77 V (region *bc*) and then gradually decreases to 1 V (region *cd*). However, the amount of lithium inserted in the region *ab* is found to be different in the first discharge cycle for TC400 compared to T100 and T400. Region *ab* comprises of formation of solid solution domain of anatase TiO_2 and Li_xTiO_2 and lithium storage in *ab* is dependent on the particle size (12, 37). However, in the present study such kind of precise size dependence could not be observed. The storage of lithium for TC400 corresponding to this region (region a_3b_3, Figure 2c) is 0.09 mol Li per TiO_2, whereas it is 0.15 mol Li per TiO_2 for both of T100 (region a_1b_1, Figure 2a) and T400 (region a_2b_2, Figure 2b). The amount of lithium storage in this region is constant from second discharge cycle onward for T100 and T400. The capacity loss observed in this region in the first discharge cycle for both of T100 and T400 suggest that some of the Li ions residing in this solid solution domain can not be retrieved in reversible manner. In case of TC400, capacity loss in this region is significantly less. In ref 12, it was discussed that nanostructuring increases the capacity associated with region *ab* at the cost of the capacity in the plateau region (region *bc*). However, we observed that carbon coating over TiO_2 nanoparticles in addition to an increase in particle size can increase the lithium storage on the plateau minimizing the lithium storage in region *ab*. The potential plateau region *bc* signifies a two phase electrochemical reaction where phase transition from Li-poor titanate to Li-titanate ($Li_{0.5}TiO_2$) occurs (9, 38, 39). The width of this biphasic region corresponds to the number of lithium ions inserted into the available interstitial octahedral sites in anatase structure based on the Faradaic mechanism and it is observed to be dependent on the particle size (37) as well as on the carbon coating. Cava et al. (38) and Murphy et al. (39) had shown from neutron diffraction studies of the anatase TiO_2 to $Li_{0.5}TiO_2$ phase transformation that Li^+ ions reside on the octahedral sites. C. L. Olson et al. (40) also showed through atomistic simulation techniques that the octahedral holes are the most energetically favorable sites for lithium storage in anatase TiO_2. About 0.27 mol of Li per TiO_2 is being intercalated in the plateau region corresponding to a discharge capacity of around 90 mA h g^{-1} in the first discharge cycle for T400 (region b_2c_2, Figure 2b) and TC400 (region b_3c_3, Figure 2c), whereas it is 0.20 mol of Li per TiO_2 for T100 corresponding to a discharge capacity of around 70 mA h g^{-1} (region b_1c_1, Figure 2a). Although the capacity in the plateau region (*bc*) of the first discharge cycle is the same for both T400 and TC400, a significant increase in the width of this plateau region (*bc*) in TC400 can be very well observed in the 30th discharge cycle as shown in Figure 2d. T400 and TC400 exhibited the same discharge capacity at the plateau probably because of their identical particle size. Nanostructuring or a decrease in particle size increases the surface to volume ratio and eventually there is a decrease in the overall available interstitial octahedral sites for Li insertion. The surface area of T100 ($\sim$240 m^2 g^{-1}) is quite high compared to T400 ($\sim$ 85 m^2 g^{-1}) and TC400 ($\sim$ 100 m^2 g^{-1}), and therefore most of the atoms lie near or on the surface, which subsequently decreases the available interstitial octahedral sites in T100. Consequently, we observed lower lithium storage in the plateau region of T100 compared to T400 and TC400. After all the available interstitial octahedral sites inside the TiO_2 crystallites are filled at the potential of 1.77 V, lithium storage takes place in the sloped region in between 1.77 to 1 V vs Li^+/Li (region *cd*). The lithium storage in this region is merely associated with the available surface states of TiO_2 crystallites (37). The surface layer generates states at potentials negative from the flat band (41), so Li ions are further inserted into the surface layer under the influence of the external force of the electric field in the region *cd*. Theoretical investigations carried out by A. Stashans et al. described that with decrease in the crystallite size the energy levels accessible to the material broaden and a wide voltage distribution at which the electrochemical reaction take place appears (42). Therefore, the discharge curve in the region *cd* appears to be a long sloped region. About 0.49 mol of Li per TiO_2 is being intercalated in the region *cd* corresponding to a discharge capacity of 163 mA h g^{-1} in the first discharge cycle for T100. For T400 and TC400, it is 0.36 and 0.44 mol of Li per TiO_2 corresponding to discharge capacities of 122 (region c_2d_2, Figure 2b) and 149 mA h g^{-1} (region c_3d_3, Figure 2c), respectively. We observed that with increase in surface area the lithium storage increases in

region *cd* in accordance with the reported literature (12, 37). However, in spite of having identical primary particle size of T400 and TC400, lithium storage in region *cd* is higher for TC400. It can be anticipated that the difference might arise because of the different amount of lithium storage in T400 and TC400 in the initial region of the discharge, i.e., region *ab* and the occurrence of such difference is merely because of the surface modification by the amorphous carbon.

The cycle stability and rate capability (Figure 4) can be described in terms of the particle size and more prominently on the carbon coating. TC400 exhibit superior cycle stability and rate capability in comparison to T100 and T400. It has been observed that there is negligible change in the initial sloped region between 1 and 1.89 V in the charging curve upon cycling which is just the Li removal process of the Li insertion between 1.77 and 1 V in TiO_2 crystallites (Figure 2a−c), which signifies that the Li ions stored in the surface states are highly reversible because of shorter diffusion time required by the lithium ions to come out from the surface. The major capacity loss in all cases is mainly attributed to the loss resulting from the plateau region (region *bc*). Comparison of the 30th discharge cycle profile of all the materials shown in Figure 2d indicates that the loss in the plateau (region *bc*) during repeated cycling is more severe for T100 and T400 compared to TC400. During initial cycles, T400 (particle size ∼10 nm) accommodates a higher amount of lithium ions in the plateau region (region *bc*) because of the lower surface:volume ratio; because storage in the plateau corresponds to lithium storage in the octahedral sites (38−40), it can be interpreted that the Li ions inserted into the bulk are gradually trapped and lose their reversibility during cycling. Theoretical investigations have also revealed that the connection between TiO_6 octahedra is severely distorted during Li ion insertion in the anatase framework, which resulted in Li ion trapping (43). The beneficial effect of carbon coating on cycle stability and high rate performance can be observed in case of TC400 (particle size ∼10 nm) (Figures 2c and 4). The plateau region contributes 47% of the total capacity in the 30th discharge cycle for TC400, whereas it is 39 and 36% for T400 and T100, respectively (Figure 2d). This relative enhancement in storage capacity in TC400 can be explained qualitatively on the basis of enhanced electronic conductivity and structural stability provided by the homogeneous carbon layer to the anatase TiO_2 nanocrystallites during lithium insertion/removal. The HRTEM image shown in Figure 3f also reflects the structural stability provided by the carbon shell to the TiO_2 nanocrystallites. To further corroborate the lithium trapping phenomenon, electrode materials were investigated in steps via ex situ XRD (6, 34, 35, 44) shown in Figure 5. Some new diffraction peaks (marked by upward directing arrows in Figure 5 at $2\theta = 23.83$, 39.72, and 44.39° can be observed in the first discharge cycle for all the materials. These can be identified with some of the main characteristic peaks of Li-titanate phase (Li_xTiO_2, $0.25 \leq x \leq 0.7$) (JCPDC No. 76−1974) (34, 45). It must be noted here that the broadening of peaks due to smaller crystallite size and overlapping of peaks of anatase TiO_2 and Li-titanate phase made it difficult to identify the other peaks of Li-titanate. The Li-titanate diffraction peaks disappeared in the first charge cycle for all the materials signifying that the structural changes accompanying Li insertion in the pristine materials are completely reversible. However, the XRD pattern taken after the 30th charge cycle for T100 and T400 shows Li-titanate characteristic peaks which are not observed for TC400. It can be interpreted that some of the inserted Li ions are getting trapped gradually in T400 and T100 during repeated cycling. On the other hand, in the case of TC400, we believe that because of the presence of the conducting carbon interface, the mobility (46) of the conducting species increases, leading to minimal trapping of Li in the anatase framework and consequently leading to disappearance of Li-titanate diffraction peaks. We would like to mention here that in situ structural investigations as performed in refs 46−48 would be a better alternative. However, at the present juncture, we are unable to do such experiments, as this is beyond our scope.

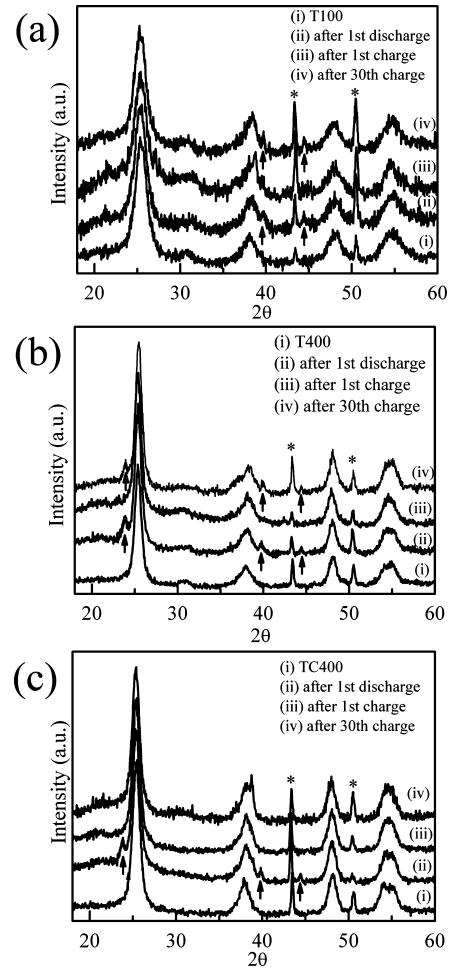

FIGURE 5. Ex situ X-ray diffraction patterns for (a) T100, (b) T400, and (c) TC400. The upward directing arrows indicate the characteristic diffraction peaks of Li-titanate phase. An * corresponds to diffraction peaks from the Cu current collector under the anode electrode film.

Figure 6 shows the cyclic voltammogram (CV) in the voltage range of 1−2.5 V for T100, T400 and TC400 at a

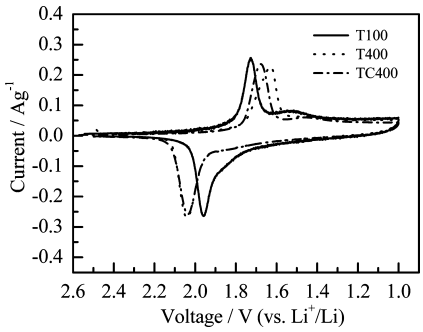

FIGURE 6. Cyclic voltammetry (CV) curves of T100, T400, and TC400 at a scan rate of 0.1 mV s^{-1}.

scan rate of 0.1 mV s^{-1}. Only one pair of distinct cathodic (insertion)/anodic (removal) peaks can be observed. Though there are no appreciable changes in the magnitude of peak currents, the peak separations are different in all cases. The peak separation is lowest (0.23 V) for T100 (particle size ~5.6 nm) which signifies that lithium insertion-removal process is more facile in case of smaller TiO_2 crystallites. M. Grätzel and his co-workers identified that kinetically favored "surface" states as primary sites for lithium insertion in TiO_2 (49). Since the surface area of T100 is quite large (~ 240 m^2 g^{-1}), the overpotential required for the transformation of TiO_2 to Li_xTiO_2 is lower. On the other hand, higher peak separation (0.41 V) is observed for T400 (particle size ~10 nm). Though the primary particle size of TC400 is identical to T400, the observed peak separation (0.36 V) is lower than T400. It signifies that the carbon coating significantly reduces the corresponding polarization resistance of the electrode/electrolyte interface in the cell. A similar phenomenon occurring because of the carbon coating has been observed in the reported literature (28, 50). Therefore, nanostructuring along with conductive coating improves the performance of lithium storage materials.

4. CONCLUSIONS

We have demonstrated here quite convincingly the role of nanostructuring and amorphous carbon coating on the lithium storage and insertion kinetics in anatase TiO_2. The results indicate that nanostructuring seems to be not the only criteria for improved cyclic stability or higher lithium storage, but coating the active particles by a conductive phase such as the amorphous carbon can significantly influence the performance of the active material. This is vividly observed in the case of better cyclability and rate capability performance of TC400 compared to T400. The carbon coating suppresses particle agglomeration and growth and provides better electronic conductivity. Additionally, the carbon coating influences the lithium insertion kinetics in anatase TiO_2 causing facile lithium insertion-removal and provides structural stability minimizing lithium trapping sites. Higher benefits of carbon coating can be obtained for even smaller-sized particle than obtained in case of TC400. We envisage that integration of a thin layer of homogeneous conductive phase in various nanostructured (e.g., nanotubes, nanorods, hollow/solid nanospheres, etc.) electrode materials will result in additional improvements in the performance of lithium ion batteries.

Acknowledgment. The authors thank I. S. Jarali (SSCU, IISc. Bangalore) for TGA and BET measurements; Sarath Kumar and A. Mandal (INI, IISc., Bangalore) for TEM and CEN; IISc, Bangalore, for glovebox facilities.

Supporting Information Available: X-ray diffraction patterns, thermogravimetry analysis (TGA), nitrogen adsorption/desorption isotherms, pore size distributions, and AC impedance spectra (SEI formation) for all the materials. This material is available free of charge via the Internet at http://pubs.acs.org.

REFERENCES AND NOTES

(1) Linsebigler, A. L.; Lu, G.; Yates, J. T. *Chem. Rev.* **1995**, *95*, 735.
(2) O'Regan, B.; Grätzel, M. *Nature* **1991**, *353*, 737.
(3) Mor, G. K.; Varghese, O. K.; Paulose, M.; Mukherjee, N.; Grimes, C. A. *J. Mater. Res.* **2003**, *18*, 2588.
(4) Yang, Z.; Choi, D.; Kerisit, S.; Rosso, K. M.; Wang, D.; Zhang, J.; Graff, g.; Liu, J. *J. Power Sources* **2009**, *192*, 588.
(5) Wang, K.; Wei, M.; Morris, M. A.; Zhou, H.; Holmes, J. D. *Adv. Mater.* **2007**, *19*, 3016.
(6) Armstrong, G.; Armstrong, A. R.; Canales, J.; Bruce, P. G. *Electrochem. Solid-State Lett.* **2006**, *9* (3), A139.
(7) Guo, Y. G.; Hu, Y. S.; Maier, J. *Chem. Commun.* **2006**, 2783.
(8) Ferg, E.; Gummow, R. J.; Dekock, A.; Thackeray, M. M. *J. Electrochem. Soc.* **1994**, *141*, L147.
(9) Jansen, A. N.; Kahalan, A. J.; Kepler, K. D.; Nelson, P. A.; Amine, K.; Dees, D. W.; Vissers, D. R.; Thackeray, M. M. *J. Power Sources* **1999**, *81*, 902.
(10) Dambournet, D.; Belharouak, I.; Amine, K. *Chem. Mater.* **2010**, *22*, 1173.
(11) Wagemaker, M; Borghols, W. J. H.; Mulder, F. M. *J. Am. Chem. Soc.* **2007**, *129*, 4323.
(12) Sudant, G.; Baudrin, E.; Larcher, D.; Tarascon, J. M. *J. Mater. Chem.* **2005**, *15*, 1263.
(13) Balaya, P.; Bhattacharyya, A. J.; Jamnik, J.; Zhukovskii, Yu-F; Kotomin, E. A.; Maier, J. *J. Power Sources* **2006**, *159*, 171.
(14) Abayev, I.; Zaban, Z.; Santiago, F. F.; Bisquert, J. *Phys. Stat. Sol. (A)* **2003**, *196*, R4.
(15) Earle, M. D. *Phys. Rev.* **1942**, *61*, 56.
(16) Yamada, H.; Bhattacharyya, A. J.; Maier, J. *Adv. Funct. Mater.* **2006**, *16*, 525.
(17) Guo, Y. G.; Hu, Y. S.; Sigle, W.; Maier, J. *Adv. Mater.* **2007**, *19*, 2087.
(18) Liu, J.; Li, W.; Manthiram, A. *Chem. Commun.* **2010**, *46*, 1437.
(19) Liu, J.; Manthiram, A. *Chem. Mater.* **2009**, *21*, 1695.
(20) Erjavec, B.; Dominko, R.; Umek, P.; Sturmb, S.; Pejovnik, S.; Gaberscek, M.; Jamnik, J. *Electrochem. Commun.* **2008**, *10*, 926.
(21) Erjavec, B.; Dominko, R.; Umek, P.; Sturm, S.; Pintar, A.; Gaberscek, M. *J. Power Sources* **2009**, *189*, 869.
(22) Jamnik, J.; Dominko, R.; Erjavec, B.; Remskar, M.; Pintar, A.; Gaberscek, M. *Adv. Mater.* **2009**, *21*, 1.
(23) Erjavec, B.; Dominko, R.; Umek, P.; Sturmb, S.; Pejovnik, S.; Gaberscek, M.; Jamnik, J. *Electrochem. Commun.* **2008**, *10*, 926.
(24) Patey, T. J.; Hintennach, A.; La Mantia, F.; Novák, P. *J. Power Sources* **2009**, *189*, 590.
(25) Das, S. K.; Darmakolla, S.; Bhattacharyya, A. J. *J. Mater. Chem.* **2010**, *20*, 1600.
(26) Chen, J. S.; Cheah, Y. L.; Chen, Y. T.; Jayaprakash, N.; Madhavi, S.; Yang, Y. H.; Lou, X. W. *J. Phys. Chem. C* **2009**, *113*, 20504.
(27) Ghosh, M.; Pralong, V.; Wattiaux, A.; Sleight, A. W.; Subramanian, M. A. *Chem. Asian. J.* **2009**, *4*, 881.
(28) Pfanzelt, M.; Kubiak, P.; Hörmann, U.; Kaiser, U.; Wohlfahrt-Mehrens, M. *Ionics* **2009**, *15*, 657.
(29) Sing, K. S. W.; Everett, D. H.; Haul, R. A. W.; Moscou, L.; Pierotti, R. A.; Rouquerol, J.; Siemieniewska, T. *Pure Appl. Chem.* **1985**, *57*, 603.
(30) Wang, Q.; Li, H.; Chen, L.; Huang, X. *Carbon* **2001**, *39*, 2211.
(31) Barrett, E. P.; Joyner, L. G.; Halenda, P. P. *J. Am. Chem. Soc.* **1951**, *73*, 373.
(32) Kresge, C. T.; Leonowicz, M. E.; Roth, W. J.; Vartuli, J. C.; Beck,

J. S. *Nature* **1992**, *359*, 710.
(33) Kavan, L.; Grätzel, M.; Rathousky, J.; Zukal, A. *J. Electrochem. Soc.* **1996**, *143*, 394.
(34) Luca, V.; Hanley, T. L.; Roberts, N. K.; Howe, R. F. *Chem. Mater.* **1999**, *11*, 2089.
(35) Ohzuku, T.; Kodama, T. *J. Power Sources* **1985**, *14*, 153.
(36) Huang, S. Y.; Kavan, L.; Exnar, I.; Gratzel, M. *J. Electrochem. Soc.* **1995**, *142*, L142.
(37) Jiang, C.; Wei, M.; Qi, Z.; Kudo, T.; Honma, I.; Zhou, H. *J. Power Sources* **2007**, *166*, 239.
(38) Cava, R. J.; Murphy, D. W.; Zahurak, S. M.; Santoro, A.; Roth, R. S. *J. Solid State Chem.* **1984**, *53*, 64.
(39) Murphy, D. W.; Cava, R. J.; Zahurak, S. M.; Santoro, A. *Solid State Ionics* **1983**, *9*, 413.
(40) Olson, C. L.; Nelson, J.; Islam, M. S. *J. Phys. Chem. B* **2006**, *110*, 9995.
(41) van de Krol, R.; Goossens, A.; Schoonman, J. *J. Phys. Chem. B* **1999**, *103*, 7151.
(42) Stashans, A.; Lunell, S.; Bergstrom, R. *Phys. Rev. B* **1996**, *53*, 159.
(43) Nuspl, G.; Yoshizawa, K; Yamabe, T. *J. Mater. Chem.* **1997**, *7*, 2529.
(44) Ohzuku, T.; Takehara, Z.; Yoshizaw, S. *Electrochim. acta* **1979**, *24*, 219.
(45) Wagemaker, M.; van de Krol, R.; Kentgens, A. P. M.; van Well, Ad A.; Mulder, F. M. *J. Am. Chem. Soc.* **2001**, *123*, 11454.
(46) Lafont, U.; Carta, D.; Mountjoy, G.; Chadwick, A. V.; Kelder, E. M. *J. Phys. Chem. C* **2010**, *114*, 1372.
(47) van de Krol, R.; Goossens, A.; Meulenkamp, E. A. *J. Electrochem. Soc.* **1999**, *146* (9), 3150.
(48) Hardwick, L. J.; Ruch, P. W.; Hahn, M.; Scheifele, W.; Kötz, R.; Novák, P. *J. Phys. Chem. Solids* **2008**, *69*, 1232.
(49) Krtil, P.; Fattakhova, D.; Kavan, L; Burnside, S; Grätzel, M. *Solid State Ionics* **2000**, *135*, 101.
(50) Fu, L. J.; Liu, H.; Zhang, H. P.; Li, C.; Zhang, T.; Wu, Y. P.; Holze, R.; Wu, H. Q. *Electrochem. Commun.* **2006**, *8*, 1.

AM1003409